Implementation of a Wollaston Interferometry Diagnostic on OMEGA EP

Introduction

The characterization of electron density in laser-plasma experiments is an area of great interest in the field of inertial confinement fusion,[1] as well as in many other fields of high-energy-density (HED) physics.[2] Modeling and quantifying the coronal plasma density profile of a laser-ablated target can serve to account for and mitigate hydrodynamic instabilities that reduce the efficiency of laser-driven fuel compression.[3] Quantitative characterization of HED plasma densities using interferometry is well documented.[4–6] Relatively high plasma densities of the order of 10^{20} cm^{-3} or above often require diagnostics that measure the gradient of phase (through refraction angle[7]) rather than phase itself. Measuring phase directly provides results with significantly less uncertainty at lower densities (<10^{20} cm^{-3}).

The most-common configurations for interferometry are typically whole-beam interferometers such as the Michelson or Mach–Zehnder.[4,5] However, as a result of the complexity and size of the OMEGA EP Laser System and target chamber, it is not possible to split the probe beam before the laser–target interaction and recombine after. Therefore, a single split-beam configuration is required. Here, the laser–plasma interaction to be probed is situated in one half of the probe beam, while the other half is used as a reference for phase. After the interaction, an optical system interferes the two halves of the probe beam to obtain phase information. A Wollaston prism configuration was chosen for this role principally because this configuration lacks significant alignment and stability problems, and allows the user significant freedoms in experimental design.[6]

The Wollaston prism configuration and similar Nomarski configurations are a common means of single-beam interferometry,[8,9] particularly for the characterization of electron density in short-pulse, laser-driven plasmas.[5,6] The design described here is unique in that it decouples fringe spacing from the field of view (FOV), magnification, and imaging resolution. As a result, these three quantities are held constant—as determined by the diagnostic's design—while fringe spacing and the beam-splitting angle may be freely chosen by the user. This freedom is advantageous for large-scale user facilities, such as OMEGA EP, wherein robust diagnostics with as few moving parts as possible are preferred.

Background

The Wollaston interferometer functions principally by use of a birefringent crystal—in this case quartz—out of which two wedged prisms are cut at a wedge angle α, rotated by 90° with respect to each other, and cemented together, as shown in Fig. 154.54. A beam incident into this prism is decomposed into its *s* and *p* polarizations as a result of the differing refrac-

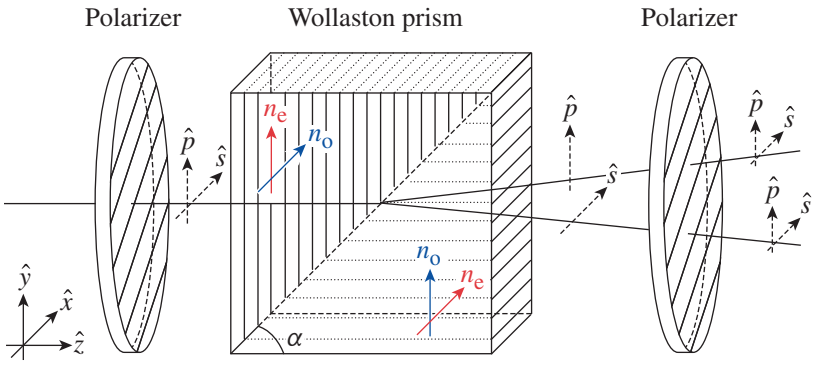

E27257JR

Figure 154.54
A schematic of the three main components in a Wollaston interferometer and their respective effects on an input beam of randomly polarized light. In the first prism, the n_o and n_e axes are oriented along the *x* and *y* directions, respectively. The opposite is true for the second prism. Both polarizers are oriented for polarization transmission along the axis 45° between *x* and *y*.

tive indices experienced by light along the x and y directions as drawn in Fig. 154.54. At the back surface of the prism, two distinct beams will emerge orthogonally polarized and angularly separated. To ensure all input beams have equal components s and p when entering the prism, a polarizer is placed before the prism at 45° with respect to the optical axis. An additional polarizer, parallel to the first, is placed after the prism to select the polarization component of each output beam again at 45°, allowing the two beams to interfere.

Figure 154.55 shows a schematic of the optical system used on OMEGA EP to implement the Wollaston interferometer. Although the presence of the first polarizer ensures that only beams with equal parts s and p will reach the prism, an input beam that is not already polarized along the 45° axis will be partially absorbed by this polarizer. To avoid this unnecessary beam attenuation, a half-wave plate (HWP) is placed directly before the first polarizer angled at

$$\theta_{\mathrm{HWP}} = \frac{\theta_{\mathrm{in}} + \theta_{\mathrm{pol}}}{2}, \tag{1}$$

where θ_{in} is the angle of the input beam's polarization and θ_{pol} is the angle of the first polarizer (all angles measured counterclockwise with respect to the x axis). Assuming the input beam is linearly polarized, a HWP oriented at this angle will rotate the input polarization to match that of the first polarizer. After rotation, any remaining ellipticity in the beam will be eliminated by the first polarizer, ensuring equal beam irradiances, resulting in high fringe contrast.

Considering now an input probe beam of appreciable width originating from infinity, a collection lens and a focusing lens may be used in conjunction to form two distinct images of the beam. The separation of these images is a function of the deviation angle between the two polarizations as they exit the prism. The deviation angle is itself a function of the birefringence of the crystal and the wedge angle of the prism. Therefore, the crystal and wedge angle may be chosen such that the two beams only partially overlap. If Region A represents the half of the beam above the optical axis and Region B represents the half below, the design parameters of the prism may be chosen such that Region A of one image overlaps onto Region B of the other, thereby creating a split-beam interferometer.

Use of this type of interferometer requires the plasma under study to be completely confined to one half (Region A or B) of the probe beam. To change the angle at which the probe beam is split, the Wollaston prism may be rotated about the z axis from 0° to 90°, allowing for flexibility in the design of the laser-plasma experiment. The two polarizers should be rotated by the same amount to provide the Wollaston with equal parts s and p and to select the output polarization of the greatest magnitude. For this reason, the two polarizers are mounted on the same rotation stage as the prism. To maintain the condition of minimal beam attenuation at the first polarizer, the HWP should be rotated accordingly [see Eq. (1)]—at half the angle of the rotation of the Wollaston—to accommodate the new angle of the polarizer.

The key attribute of this design is the ability to easily vary fringe spacing without affecting beam overlap, magnification, or imaging resolution. As can be seen in Fig. 154.55, a collimated probe beam creates two point sources that are situated just to the left of the final focus lens. These point sources interfere to provide the fringes observed in the region of image overlap at the image plane. When two point sources interfere, fringes form at discrete angles, and the fringe separation observed is inversely proportional to the spacing between the two sources. When a lens is used to focus the fringes, these discrete angles

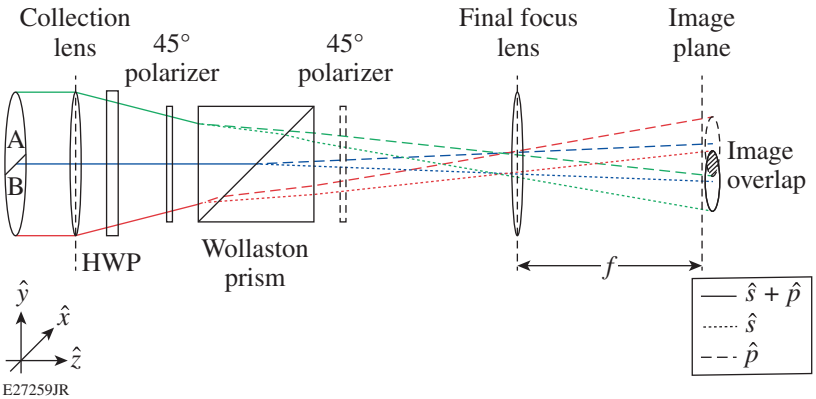

Figure 154.55
Schematic demonstrating how spatially separated Regions A and B may be overlaid and may interfere with one another. It should be noted that in this sketch the beam polarizations are drawn as if the second polarizer were inactive in order to better demonstrate how each polarization propagates through to the image plane. Each ray is colored according to the region of space from which it originates: green represents Region A, red represents Region B, and blue represents the midpoint between the two regions.

are converted to discrete positions in space. Since the angles presented to the lens do not depend on the distance between the point sources and the lens, the fringe density is independent of where the point sources fall along the z axis (referring to Fig. 154.55). Applying the small angle approximation for two-point-source interference,[10] the fringe separation s is

$$s = \frac{\lambda f}{d}, \tag{2}$$

where λ is the wavelength of the probe beam, f is the focal length of the final focus lens, and d is the distance between the two point sources. In this system, the Wollaston prism is responsible for the point-source separation. The prism imparts an angle between the gently converging rays of s- and p-polarized light, and these now deviated rays are allowed to propagate over some distance in the z direction, creating a separation between the rays in the y direction (as seen in Fig. 154.55) when they reach the focus of the collection lens. Altering the z distance over which these rays propagate—by moving the prism along the z axis—will linearly affect the separation between the sources. Knowing now that z is proportional to d, where z is the distance over which the deviated rays are allowed to propagate before reaching a focus, Eq. (2) dictates that s is *inversely proportional* to z. Therefore, fringe spacing is variable and may be changed simply by adjusting the position of the prism with respect to the final focus lens.

The final image overlap, by contrast, is purely a function of the angle of deviation between the two beams exiting the prism. As the prism imparts the same angle regardless of its position, moving the prism along the z axis alters the fringe spacing without affecting the image overlap. Magnification is also independent of the fringe spacing because it is simply the ratio of the f number of the final focus lens over that of the collection lens. Moving the prism does not change either f number and therefore does not affect magnification. Finally, it should also be noted that the fringe density is independent of resolution; this optical system is diffraction limited, so the resolution is limited only by the f number of the collection lens.

It may also be noted that this design is free of the aberrations (spherical, astigmatism, etc.) introduced in past designs[5,6,8,9] by focusing and forming an image through the prism. Looking to Fig. 154.55, an image is formed only by the final focus lens and notably not by the collection lens. For an object placed at the front focus of the collection lens, each point will convey a bundle of rays (not drawn in Fig. 154.55) that travel *collimated* through the prism, avoiding the typical aberrative effects of imaging through a thick prism.

Experimental Setup

In the OMEGA EP Laser System, the 1054-nm output of an Nd:glass laser is sent through an IR transport system and frequency quadrupled[11] to yield a 5-mm-diam 4ω probe beam expanding at $f/25$. This beam is then passed through the target chamber center (TCC), where the laser–plasma interaction takes place. The beam is collected at $f/4$, and imaged downstream using a catadioptric telescope and transport system[11] to the 4ω diagnostic table, where it encounters the system shown in Fig. 154.55 before finally reaching a charge-coupled device (CCD). Figure 154.56 demonstrates how the field of view (FOV) of this system is defined by the intersection between Regions A and B of the two overlapping images, where fringes are clearly visible. This region is approximately 1.2×1.6 mm at TCC.

The magnification of this system was measured with the alignment grid shown in Fig. 154.56 and found to be 13.5, yielding a pixel pitch at the CCD of 1 μm/pixel. At this magnification, an imaging resolution of 5 μm is attained.

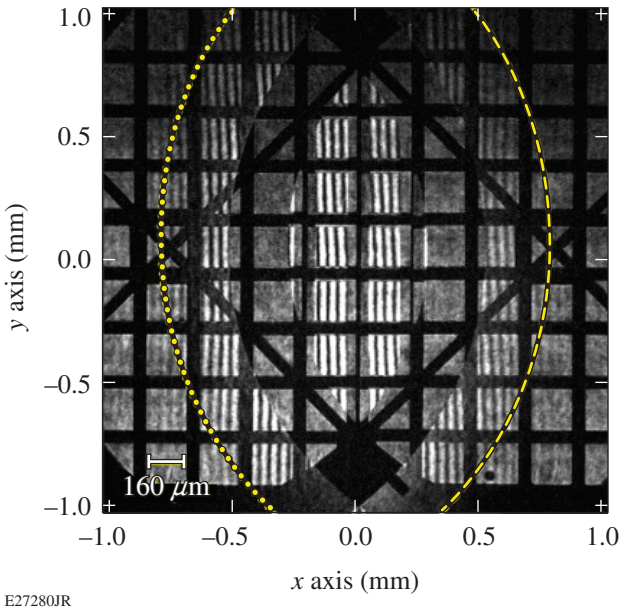

Figure 154.56
Interferogram produced by a 4ω alignment grid placed at target chamber center (TCC). The dashed and dotted yellow lines represent the edges of the two overlaid images produced by the interferometer. The features on this grid are of a known size (160×160 μm) and were used to calibrate the axes and define the field of view at TCC.

Since the fringe spacing is a function of the Wollaston prism's position, it may be altered over a definite range. This range was tested with the Wollaston prism mounted on an optical rail. Figure 154.57 shows two cases [(a) and (b)] in which the position of the Wollaston prism along the rail differs significantly to produce relatively broad (76 μm/fringe) and fine (17 μm/fringe) fringe spacings. In Fig. 154.57(c), six experimental images of differing fringe spacings were analyzed and plotted against their corresponding prism positions. From Eq. (3), it is clear that fringe spacing is inversely proportional to the z distance over which the deviated s and p beams propagate, which is consistent with an inverse trend between measurements of prism position and fringe spacing. By this relation, fringe spacing may be varied from ~17 μm/fringe to 76 μm/fringe.

Data Retrieval and Analysis

In general, the analysis of interferometry for the purpose of yielding plasma density information occurs in two steps: phase retrieval and density extraction. In the first step, the variations in fringe spacing of an interferogram are converted to repeating variations in phase. These phase variations, each occurring over an interval of $-\pi$ to π, are "unwrapped" to form a continuous map of phase. The phase from a reference interferogram, with no phase object present, is subtracted to account for any offsets or aberrations in the optical system. After retrieving phase information, a relation is made between the phase accrued when light passes through a plasma and that plasma's electron density distribution. With this relation, an axisymmetric 3-D plasma density can be recovered.

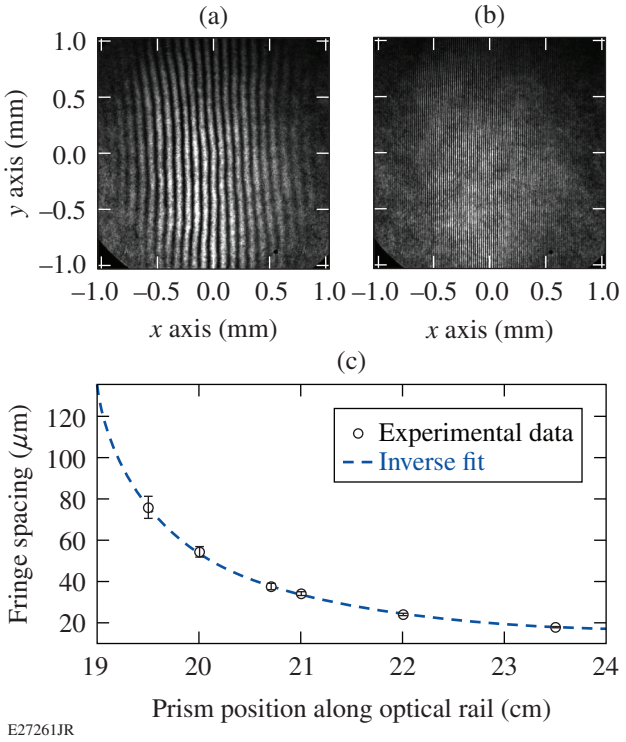

Figure 154.57
(a) Interferogram produced when the Wollaston prism is at a position of 19.5 cm along the optical rail; fringe spacing: 76±5 μm. (b) Interferogram produced when the prism is at position 23.5 cm; fringe spacing: 17.4±0.2 μm. (c) Plot of fringe spacing as a function of prism position. Data, drawn as black circles with vertical error bars, were taken from six experimental images with fringe spacings found programmatically to yield a standard deviation. The dashed trend curve, shown in blue, represents an inverse fit of the data.

To investigate experimental error, the phase variations in a reference interferogram with relatively moderate fringe spacing (34 μm/fringe) were analyzed, as displayed in Fig. 154.58. To retrieve the phase from this interferogram, a fast Fourier transform method[12] was used. A region of interest (ROI) was selected where valuable phase information could be retrieved [as seen in Fig. 154.58(a)], and a discrete 2-D Fourier transform of the interferogram was computed, producing a 2-D spatial frequency map $F(k_x,k_y)$. Because these fringes occur only in the x direction, all relevant phase information is contained in k_x and the frequency map $F(k_x,k_y)$ was summed in the y direction to yield $F(k)$. This now 1-D spatial frequency distribution $F(k)$ contains a dc term centered at $k = 0$, representing the slowly varying background features of the image, and two ac terms offset from $k = 0$ symmetrically, representing the sinusoidal variation of the fringes. One of these two ac terms was selected through spectral filtration and inverse Fourier transformed to create a new interferogram containing only the fringes and phase perturbations present in the original image [see Fig. 154.58(b)]. The 2-D phase angle of this new interferogram was calculated and unwrapped using a phase-unwrapping algorithm. Another reference interferogram with identical fringe spacing and image overlap was analyzed, and its 2-D phase subtracted from the 2-D phase yielded by the first. Figure 154.58(c) shows the resultant phase variations in the ROI.

As expected, the phase difference $\Delta\varphi$ retrieved from an interferogram with no phase object present looks like experimental noise centered around $\Delta\varphi = 0$. The standard deviation of this phase noise was found to be ±0.4 rad.

Using the geometrical optics approximation for slowly varying media,[13] the measured phase difference in the interferogram can be expressed as a function of density integrated along a chord through the plasma:

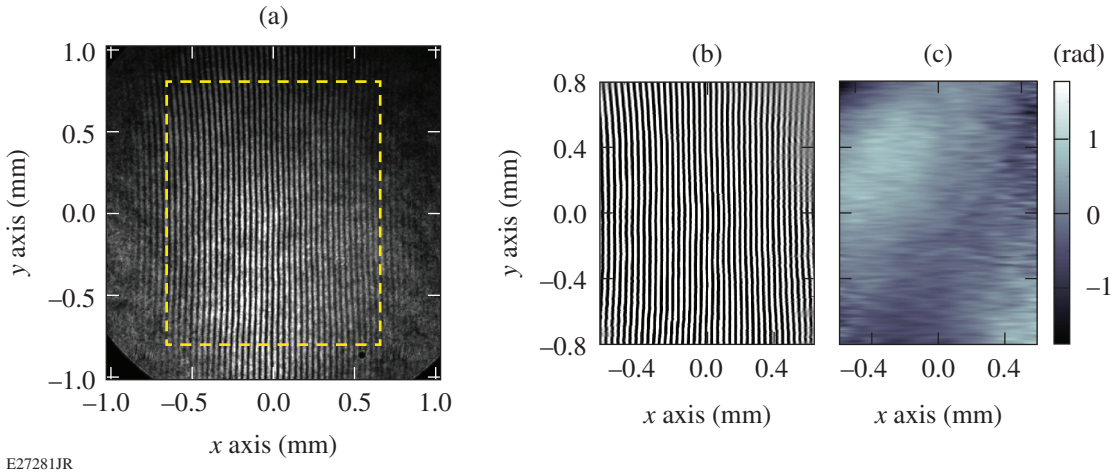

Figure 154.58
(a) The region of interest (ROI), denoted by dashed yellow lines, shown within the full interferogram as seen by the charge-coupled device. This interferogram was produced at rail position 21.0 cm, with approximate fringe spacing 34 μm/fringe. (b) The ROI, after having its dc term filtered. (c) The phase retrieved from the ROI, subtracted by the phase of another identically treated interferogram.

$$\Delta\varphi = \frac{-\pi}{\lambda n_c}\int n_e \mathrm{d}l, \tag{3}$$

where n_c is the critical plasma density for the probe beam $\left(n_c \equiv 4\pi^2 c^2 m\epsilon_0 / \lambda^2 e^2\right)$, λ is the wavelength of the probe beam, n_e is the electron (plasma) density, dl is the differential unit length through the plasma, m is the mass of an electron, and e is the electron charge. Assuming that the plasma under study is axisymmetric, Eq. (3) is Abel inverted[14] to extract the plasma density profile from the phase.

To gauge the range over which plasma density may be accurately measured using this diagnostic, a "synthetic" axisymmetric plasma density profile was used. By analyzing a phase map with a *known* density profile, it is possible to quantify the propagation of phase error through Abel inversion and to characterize an uncertainty in density. Figure 154.59(a) shows a model plasma density profile typical of coronal plasmas from a flat target.[15] The profile was integrated to yield phase by using Eq. (3). This phase was then directly Abel inverted and compared to the original density distribution to ensure agreement and confirm the validity of the method. The average percent error across the ROI caused by Abel inversion alone was found to be ~4%. The phase noise found previously [see Fig. 154.58(c)] was then added to the synthetic phase map [Fig. 154.59(b)] and Abel inverted to yield a plasma density distribution with quantifiable error resulting from noise [Fig. 154.59(c)]. The average error in density over this region was calculated to be $\pm 7 \times 10^{17}$ cm^{-3}. As can be seen in Fig. 154.59(d), the added phase noise does not significantly impact densities of the order of 10^{19} cm^{-3} and above but quickly deteriorates data where density reaches below 3×10^{18} cm^{-3}.

Conclusion

A Wollaston interferometer was built and implemented onto the 4ω diagnostic table of OMEGA EP. The interferometer uses a Wollaston prism to overlap two regions of a single probe beam, resulting in fringes in an FOV of 1.2 × 1.6 mm at TCC. The design of the diagnostic allows for unique flexibility in experimental design at large-scale fusion facilities, permitting each user to freely vary the fringe spacing (17 to 76 μm/fringe) and beam-splitting angle (0° to 90°) with no effect on FOV, magnification, or imaging resolution. Preliminary analysis has indicated that the interferometer allows the characterization of plasma density over a range of 3×10^{18} to 1×10^{20} cm^{-3} with a phase noise of approximately ±0.4 rad. Looking forward, this diagnostic will be used in conjunction with other existing diagnostics on OMEGA EP—namely angular filter refractometry (AFR)[5]—to greatly reduce experimental uncertainty in the low-density regions (~10^{19} to ~10^{20} cm^{-3}), where the data sets of both diagnostics overlap and to supplement data at densities below the current lower limit of AFR at ~10^{19} cm^{-3}.

ACKNOWLEDGMENT

This work is supported by the Department of Energy National Nuclear Security Administration under Award Number DE-NA0001944. The support of DOE does not constitute an endorsement by DOE of the views expressed in this article.

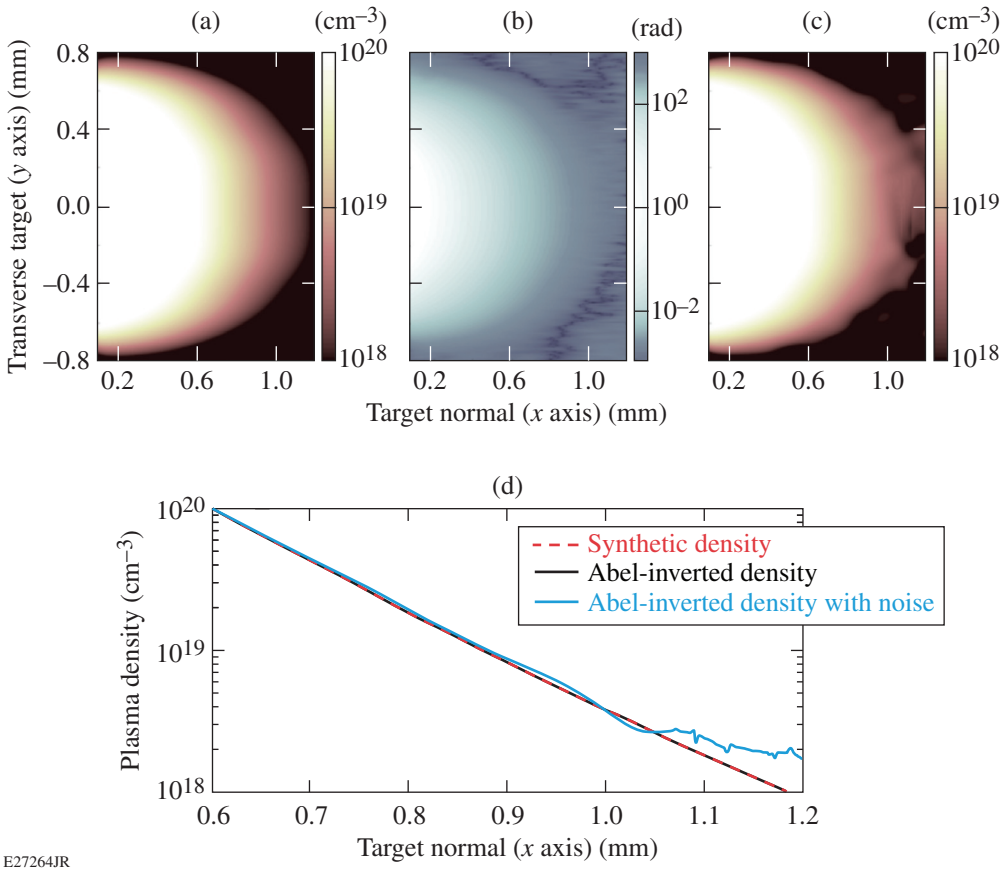

Figure 154.59

(a) An axisymmetric "synthetic" plasma density used as the phase object to be analyzed. (b) The phase yielded by integrating over the synthetic density in Fig. 154.59(a) using Eq. (3), plus the phase noise as seen in Fig. 154.58(c). (c) The density profile yielded by Abel inverting the phase in Fig. 154.59(b). (d) A series of logarithmic plasma density profiles along the target normal centered at $y = 0$ mm. The synthetic plasma density is drawn as a dashed red line, the Abel-inverted density (without noise) as a solid black line, and the Abel-inverted density with noise as a solid blue line.

REFERENCES

1. R. Betti and O. A. Hurricane, Nat. Phys. **12**, 435 (2016).
2. National Research Council (U.S.) Committee on High Energy Density Plasma Physics, *Frontiers in High Energy Density Physics: The X-Games of Contemporary Science* (The National Academies Press, Washington, DC, 2003).
3. D. T. Michel, A. V. Maximov, R. W. Short, J. A. Delettrez, D. Edgell, S. X. Hu, I. V. Igumenshchev, J. F. Myatt, A. A. Solodov, C. Stoeckl, B. Yaakobi, and D. H. Froula, Phys. Plasmas **20**, 055703 (2013).
4. I. H. Hutchinson, *Principles of Plasma Diagnostics*, 2nd ed. (Cambridge University Press, Cambridge, England, 2002), pp. 104–117.
5. S. S. Harilal and M. S. Tillack, Fusion Division, Center for Energy Research (University of California, San Diego, La Jolla, CA, 2004).
6. R. Benattar, C. Popovics, and R. Sigel, Rev. Sci. Instrum. **50**, 1583 (1979).
7. D. Haberberger, S. Ivancic, S. X. Hu, R. Boni, M. Barczys, R. S. Craxton, and D. H. Froula, Phys. Plasma **21**, 056304 (2014).
8. R. D. Small, V. A. Sernas, and R. H. Page, Appl. Opt. **11**, 858 (1972).
9. U. Kogelschatz, Appl. Opt. **13**, 1749 (1974).
10. J. Walker, D. Halliday, and R. Resnick, *Fundamentals of Physics*, 9th ed. (Wiley, Hoboken, NJ, 2011).
11. D. H. Froula, R. Boni, M. Bedzyk, R. S. Craxton, F. Ehrne, S. Ivancic, R. Jungquist, M. J. Shoup, W. Theobald, D. Weiner, N. L. Kugland, and M. C. Rushford, Rev. Sci. Instrum. **83**, 10E523 (2012).
12. M. Takeda, H. Ina, and S. Kobayashi, J. Opt. Soc. Am. **72**, 156 (1982).
13. I. H. Hutchinson, *Principles of Plasma Diagnostics*, 2nd ed. (Cambridge University Press, Cambridge, England, 2002), p. 111.
14. M. Kalal and K. A. Nugent, Appl. Opt. **27**, 1956 (1988).
15. P. Angland, D. Haberberger, S. T. Ivancic, and D. H. Froula, Rev. Sci. Instrum. **88**, 103510 (2017).